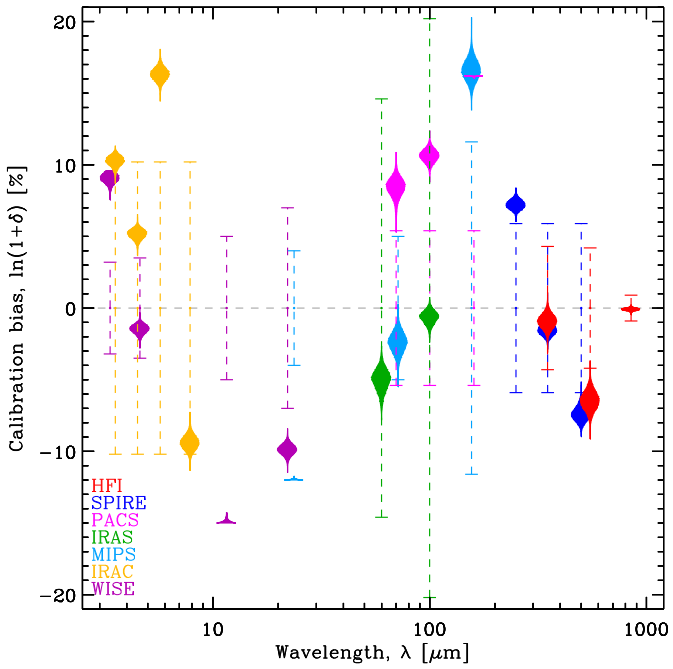

Fig. 3. Inferred calibration biases. This figure shows our inference of the calibration bias, δ, defined in Sect. 3.2.2 of G18, for each of the photometric filters in Table 1. Each instrument is color-coded. The vertical dashed error bars represent the calibration prior, that is the $\pm 1\sigma$ range given in Appendix A. The violin plots show the actual posterior PDFs of δ, for each broadband. The width of a single violin plot is proportional to the PDF as a function of δ (vertical axis).

galaxies (LTG), and irregulars, respectively, are displayed. The PDF of the SED is shown as a yellow density plot. We also show the PDF of the synthetic photometry (violin plots[13] of different colors). The comparison of this synthetic photometry to the observed flux (circles with an error bar) reflects the quality of the fit. We discuss a more thorough and technical fit quality test in Appendix D. Panel d shows the example of a galaxy where most of the fluxes are 3σ-upper limits (displayed when $F_\nu < \sigma_\nu^{\rm noise}$). When the evidence provided by the data is weak, which is the case when few detections are available, the posterior distribution becomes dominated by the prior. This is what we see here. The range spanned by this SED PDF is the extent of the prior. The global scaling of this SED is very uncertain, but its shape is realistic. This would not be the case with a nonhierarchical model.

Figure 3 shows the inference of the calibration biases, $\delta(\lambda)$, of each waveband (Sect. 2.1.3). Basically, the model fluxes are corrected by factors $1+\delta(\lambda)$. For each waveband, the dashed-line error bar represents the $\pm 1\sigma$ interval of the prior on the calibration bias. This prior is a multivariate normal distribution, centered on 0, with the covariance matrix of Eq. (A.2). As discussed in Sect. 3.1.3, besides accounting for the uncertainty in the calibration of each instrument, these coefficients can account for external contaminations and fitting residuals. We can interpret the most deviant values of Fig. 3 in this light. The posterior values of δ lying outside their $\pm 2\sigma$ prior are the following.

160 μm : both overlapping bands PACS3 and MIPS3 indicate an excess emission of about 15%. A significant fraction of this excess is likely due here to contamination by the brightest line of the ISM, $[\mathrm{C\,II}]_{158\,\mu\mathrm{m}}$. The $[\mathrm{C\,II}]_{158\,\mu\mathrm{m}}$ intensity is about $\simeq$1% the FIR (far-IR; 60–200 μm) power (Malhotra et al. 1997, 2001; Brauher et al. 2008; Cormier et al. 2015). Its contribution to the PACS3 and MIPS3 is thus expected to be a few percent, as these bands are narrower than the FIR range.

12 μm and 22 μm : the deficit could be due to a systematic difference between the size distribution of medium a-C(:H) grains implemented in THEMIS and in the diffuse ISM of these galaxies. Although the model was different, Galliano et al. (2011, Appendix A.2) had to decrease the abundance of the grains carrying the 24 μm continuum in the Large Magellanic Cloud (LMC), for a similar reason.

Apart from these deviations, the two overlapping bands WISE1 and IRAC1 indicate that the model, on average, underestimates the observations by $\simeq$10% around 3.5 μm. This could be due to either the continuum or the 3.3 and 3.4 μm features. The constraint of the size distribution of THEMIS by the SED of the Milky Way (Fig. 3 of Jones et al. 2013), has been performed with a medium resolution IRS spectrum for all a-C(:H) features, except the two in question here. The global emissivity of these features is the most uncertain of the model. We also notice that the SPIRE calibration biases go in opposite directions, while they should be partially correlated (Appendix A.5). The HFI1 and HFI2 calibration biases agree very well with SPIRE. This is the sign that there is a systematic residual proportional to the flux in this wavelength range. It could mean that the slope of THEMIS is not steep enough in the 200–500 μm range[14]. The fact that the HFI3 is almost 0 would mean that the slope flattens again longward $\simeq$800 μm. This is very speculative, but we note that this behavior is qualitatively consistent with the optical properties measured in the laboratory by Demyk et al. (2017b).

The parameters inferred with this run, for each galaxy, are given in Appendix H. We report only the parameter values and their uncertainties (mean and standard-deviation of the posterior PDF). The skewness and correlation coefficients can be retrieved from the DustPedia archive[15]. The length of the MCMC of this run is 1 000 000, where we have excluded the first 100 000 steps, to account for burn-in. The maximum integrated autocorrelation time (Eq. (43) of G18) is 65 000.

3.3. Additional runs: robustness assessment

In order to assess the robustness of our results, we have performed several additional runs, with different assumptions. We now discuss the comparison of these tests with our reference run. We focus on the derived dust mass and do not display the redundant comparisons with $\langle U \rangle$. Indeed, TIR is usually well constrained and, by model construction, TIR $\propto M_{\rm dust} \times \langle U \rangle$. We discuss the difference in $q_{\rm AF}$, when relevant. Figures 4–6 compares $M_{\rm dust}$ or $q_{\rm AF}$ derived by these tests to the same quantity derived by the reference run, $M_{\rm dust}^{\rm ref}$ and $q_{\rm AF}^{\rm ref}$, respectively. Table 3 reports some statistics on this comparison. We color code the galaxies according to their Hubble stage, T:

Early-type: $T \leq 0$ (red);
Late-type: $0 < T < 9$ (green);
Irregulars: $T \geq 9$ (blue).

3.3.1. Influence of the fitting method

Least-squares. We have fit the full sample of Sect. 2 with the physical model of Sect. 3.1, using a standard least-squares method (cf. Appendix C of G18). The goal of this run is to

[13] Violin plots are 90°-rotated histograms.

[14] We do not implement the evolution of the grain properties with accretion and coagulation that could account for a steeper far-IR slope.

[15] http://dustpedia.astro.noa.gr